



Hollow carbon sphere encapsulated nickel nanoreactor for aqueous-phase hydrogenation-rearrangement tandem reaction with enhanced catalytic performance

Zhi Hu^{a,b}, Miaomiao Han^c, Chun Chen^{a,*}, Zidan Zou^{a,b}, Yue Shen^{a,b}, Zhen Fu^a, Xiaoguang Zhu^a, Yunxia Zhang^a, Haimin Zhang^a, Huijun Zhao^{a,d}, Guozhong Wang^{a,*}

^a Key Laboratory of Materials Physics, Centre for Environmental and Energy Nanomaterials, Key Laboratory of Materials Physics, Institute of Solid State Physics, HFIPS, Chinese Academy of Sciences, Hefei 230031, China

^b Science Island Branch, Graduate School of USTC, Hefei 230026, China

^c School of Science, Huzhou University, Huzhou 313000, Zhejiang, China

^d Centre for Clean Environment and Energy, Gold Coast Campus, Griffith University, Queensland 4222, Australia

ARTICLE INFO

Keywords:

Nanoreactor
Void-confinement effect
Aqueous phase
Tandem reaction

ABSTRACT

As green chemistry, aqueous-phase reactions play a vital role in modern fine chemical synthesis. Herein, an encapsulated nickel in a hollow carbon sphere (Ni@HCS) catalyst was constructed to effectively catalyze an aqueous-phase hydrogenation-rearrangement tandem (AP-HRT) reaction, in which water was employed as the solvent and reactant simultaneously. The activity is relevant to the HCS and Ni loading. The optimal Ni@HCS catalyst can release 100% furfural conversion and 99.1% cyclopentanone selectivity at 150 °C and can maintain its activity after 10 cycles of experiments. The superior catalytic performance comes from the fact that each independent Ni@HCS can be treated as an individual nanoreactor with a void-confinement effect, which not only reduces the side reactions due to the size-selective effect but also prevents active metal from leaching under harsh conditions. The reaction mechanism of FAL AP-HRT was further investigated via kinetic experiments combined with DFT calculations.

1. Introduction

With the growth of energy demand and the consumption of conventional energy, there is an urgent need to find new energy sources with large and renewable reserves. Lignocellulose, the most abundant biomass resource in the world, plays an important role in solving the crisis caused by oil depletion [1,2]. Lignocellulose can be refined into a variety of small molecule intermediates through chemical and physical methods, which can be valued up by further chemical reactions, such as hydrogenation, hydrodeoxygenation, rearrangement, etc. Furfural (FAL) is a pivotal bioderived building block transformed from lignocellulose, and it can be further converted into a series of important chemicals, such as furfuryl alcohol (FOL), tetrahydrofurfuryl alcohol (THFOL), 2-methylfuran (2-MF), levulinic acid (LA) and cyclopentanone (CPO) [3–6]. Among them, CPO is a versatile intermediate in the medicine, perfume, and rubber industries. Currently, CPO is mainly produced by the petrochemical industry, which uses high-cost feedstocks,

such as 1,6-hexanediol, cyclopentene, and adipic esters. In addition, the low selectivity of CPO is a problem to be solved urgently in traditional industrial processes [7]. Therefore, it is highly urgent and desirable for the highly selective synthesis of CPO from bio-derived ingredients.

Aqueous-phase hydrogenation has been reported to not only meet the requirements of green chemistry but can also selectively produce CPO from bio-derived FAL [8–13]. The use of water as a solvent has incomparable advantages in environmental protection and economy compared with organic solvents. Meanwhile, the hydrogenation process is often accompanied by the formation of water; thus, the aqueous environment can greatly simplify the separation and purification of the products. Nevertheless, the aqueous-phase hydrogenation of FAL toward CPO needs to be carried out under harsh reaction conditions (such as high reaction temperature) [14,15], which makes water a serious limitation to the stability of the heterogeneous catalyst. Previous studies have proven that conventional oxide supports such as γ -Al₂O₃ and SBA-15 undergo phase transitions or structural collapse at high

* Corresponding authors.

E-mail addresses: chenchun2013@issp.ac.cn (C. Chen), gzhwang@issp.ac.cn (G. Wang).

<https://doi.org/10.1016/j.apcatb.2022.121140>

Received 13 October 2021; Received in revised form 17 January 2022; Accepted 21 January 2022

Available online 25 January 2022

0926-3373/© 2022 Elsevier B.V. All rights reserved.

temperatures in aqueous solutions [16,17]. Compared with oxide, carbon material has better stability in the aqueous phase, which makes it a potential catalyst carrier. However, due to the weak interaction between the active metal component and support, the carbon-supported catalyst would face another problem: leaching and agglomeration of the active component [18–20]. In addition, under a harsh environment, the side reactions of the hydrogenation of FAL (e.g., the further hydrogenation of furan ring and the hydrodeoxygenation of furfuryl alcohol) are also difficult to control. As a result, it is a great challenge to develop a heterogeneous catalyst that has a high activity with satisfactory stability and selectivity for transforming FAL toward CPO in the aqueous phase.

Hollow structure materials have been widely investigated in heterogeneous catalysis due to their unique properties, which would induce a magical effect on the catalytic process [21]. Active component loading on different parts of the hollow shell (e.g., the outer surface, the pore structure, or the cavity) can lead to versatile catalytic behaviors due to variations in the microenvironment at different positions [22–24]. Hollow structure encapsulating active metals materials can be regarded as nanoreactors to present the void-confinement effect for tailoring the microenvironment of hollow nanoreactors [25–28]. On the one hand, active metal nanoparticles (NPs) can be dispersed and isolated by the hollow shell in each individual nanoreactor and can protect them against aggregation, sintering, and leaching to withstand deactivation under harsh preparation and reaction conditions [29]. Consequently, the hollow nanoreactor catalyst can display high activity and stability in heterogeneous catalysis, especially in liquid-phase reactions. On the other hand, similar to a molecular sieve catalyst, the pore and cavity structure of a hollow catalyst can tune the microenvironment surrounding each individual nanoreactor to display shape-selective catalysis [27]. As a result, the hollow nanoreactor catalyst can also exhibit excellent selectivity in liquid-phase heterogeneous catalysis. Xu [22] et al. prepared a FeMn@Hollow HZSM-5 nanoreactor that displayed a surprisingly high space-time yield of $1.9 \text{ g g}_{\text{Fe}}^{-1} \text{ h}^{-1}$, and this enhanced catalytic ability can be attributed to the hollow structure of the catalysts, which fully exploited the shape selectivity and aromatization ability of the HZSM-5 zeolite. Cui [28] et al. applied a ZIF-67@SiO₂-CPTES core-shell structure in the selective transfer hydrogenation of cinnamaldehyde to cinnamyl alcohol, and the catalyst afforded a 95% cinnamyl alcohol yield and maintained its activity after 5 uses. However, as mentioned, zeolite or SiO₂ based catalysts undergo phase transitions or structure collapse at high temperatures in aqueous-phase reaction systems, leading to silica-based hollow nanomaterials that may not be usable in aqueous-phase reactions.

Compared with other hollow structure materials, hollow carbon spheres (HCSs) can be used as an ideal support to deposit active metals for forming nanoreactors due to the high surface area, adjustable pore structure, inertia property, and high thermostability of HCSs. As a result, if encapsulating the active component in HCS, the aqueous-phase catalytic stability of the catalyst can be greatly improved. Recently, Dong [23] et al. successfully used the microemulsion method to encapsulate PdCu alloys in HCS, and PdCu@HCS catalysts showed good performance in liquid-phase hydrogenation. Yu [24] et al. also used SiO₂ as a template and obtained the Ru@HCS catalyst through the template sacrifice method, which displayed high imine selectivity in the nitrobenzene hydrogenation tandem reaction. These noble metal-based HCS catalysts showed attractive catalytic performance in liquid-phase reactions because of the void-confinement effect induced by the hollow structure.

Inspired by these findings, we proposed a new facile route to synthesize a non-noble nickel hollow catalyst (Ni@HCS) through a vacuum-assisted impregnation method. Under vacuum, the active Ni species could be mainly encapsulated into the void space of HCS. The shell thickness, cavity size, and Ni loading could be controllably tuned to obtain the Ni@HCS catalyst with optimal catalytic performance. The synthesized Ni@HCS catalyst was applied in the AP-HRT reaction and displayed high activity, selectivity, and stability for converting FAL into CPO. We explained this superior catalytic performance by a void-

confinement effect induced by the hollow structure of HCS. The reaction mechanism of FAL AP-HRT was further investigated via reaction dynamics and DFT calculations at the molecular and atomic levels, and the gram-scale AP-HRT reaction of FAL and other furan-based unsaturated compounds was also explored. This work offers a distinct case for designing a highly active and stable heterogeneous catalyst for an aqueous-phase tandem reaction in a green way.

2. Materials and method

2.1. Chemicals and materials

All reagents were AR pure and were used without further purification. Tetraethyl orthosilicate, resorcinol, Ni(NO₃)₂·3H₂O and furfural were purchased from Aladdin Reagent (Shanghai) Co. Ltd., anhydrous ethanol, ammonia solution, formaldehyde aqueous solution, methanol, 2-propanol, and 1-butanol were purchased from Sinopharm Chemical Reagent Co. Deionized water with a resistance larger than 18.2 MΩ used throughout the experiments.

2.2. Preparation of hollow carbon sphere

Hollow carbon spheres (HCSs) were synthesized by a sacrificial template method with SiO₂ spheres as a template. In a typical process, 3.56 ml tetraethyl orthosilicate was added into a mixture with 70 ml anhydrous ethanol and 10 ml H₂O with vigorous stirring. After mixing well, 3 ml ammonia solution was added into the above system quickly and then further stirred for 30 min. As the mixture turned to be a white suspension, 0.4 g resorcinol and 0.56 ml formaldehyde aqueous solution were added into the above mixture and stirred for another 24 h. The products were separated from the mixture by centrifugation, washed with ethanol several times, and then dried at 60 °C for 12 h. The dried samples were treated in N₂ at 700 °C for 5 h with a heating rate of 2 °C min⁻¹ to obtain C/SiO₂. After that, the SiO₂ core was removed by HF etching, and the remaining carbon shell was washed with deionized water and anhydrous ethanol and dried at 60 °C for further use. The thickness of the carbon shell can be controlled by adjusting the amount of resorcinol, and the cavity size of the HCS can be controlled by adjusting the amount of TEOS and ammonia.

2.3. Preparation of catalysts

2.3.1. preparation of Ni@HCS

Ni was embedded into the HCS by the vacuum impregnation method. In detail, a certain amount of Ni(NO₃)₂ was dissolved in 10 ml anhydrous ethanol, and then 100 mg prepared HCS was added to the above solution. The mixture was uniformly dispersed by ultrasonication and transferred into a round bottom flask. Then, the solvent was evaporated at 60 °C in a negative pressure environment using a rotary evaporator. The obtained black powder was treated in H₂/Ar (10 vol%) at 400 °C for 2 h with a heating rate of 5 °C min⁻¹ to obtain the target catalysts.

2.3.2. preparation of Ni/AC

The Ni/AC was prepared by precipitation method. In a typical process, 300 mg active carbon (AC) was dispersed in a Ni(NO₃)₂ aqueous solution at a calculated concentration. The mixture was dispersed by ultrasonication, and then a Na₂CO₃ aqueous solution was added dropwise into the mixture under vigorous stirring to maintain the pH value at 9 for 30 min. After that, the precipitate was washed with deionized water several times and dried at 60 °C for 12 h. The obtained black powder was treated in H₂/Ar (10 vol%) at 400 °C for 2 h with a heating rate of 5 °C min⁻¹ to obtain the Ni/AC catalyst.

2.3.3. preparation of Ni@AC

The preparation process of Ni@AC was similar to that of Ni@HCS, and the only change was that the HCS was changed to an equal amount

of AC.

2.4. Catalyst characterization

The crystalline structures of the catalysts were determined by Powder X-ray diffraction (XRD, Philips X Pert Pro X-ray diffractometer) using Ni-filtered monochromatic Cu K α radiation at 40 kV and 40 mA. The morphology of the products was characterized by field emission scanning electron microscopy (FESEM, SU8020) and transmission electron microscopy (TEM, JEOL-2010) with an energy dispersive X-ray spectrometer (EDS Oxford, Link ISIS). The nitrogen adsorption experiment was run at $-196\text{ }^{\circ}\text{C}$ on a Micrometrics ASAP 2020M. The Ni contents of all the catalysts were determined by inductively coupled plasma spectrometry (ICP-AES). XPS analysis was carried out on an ESCALAB 250 X-ray photoelectron spectrometer (Thermo, U.S.A.) equipped with Al K $\alpha_{1,2}$ monochromatized radiation at a 1486.6 eV X-ray source. H $_2$ -TPR analysis was carried out by a Micromeritics AutoChem II 2920 instrument.

2.5. Catalytic test

The catalytic reactions were carried out in a 25 ml stainless steel autoclave (Anhui Kemi Machinery Technology Co. Ltd). In a typical experiment, 10 mg Ni@HCS catalysts and 1 mmol reactant were introduced into the reactor with 10 ml H $_2$ O, and the mixture was dispersed evenly by ultrasound for 1 min. Then, the reactor was purged with N $_2$ several times to remove air, pressurized with a certain amount of H $_2$, heated to the desired temperature, and maintained at the temperature for a set time. After the reaction, the reactor was cooled to room temperature quickly, and the catalysts were separated by filtration using a 0.22 μm filter. In a typical recycling experiment, the catalysts were separated from the reaction system by centrifugation, washed with H $_2$ O several times, and then reused without further treatment. The products were identified by gas chromatography-mass spectrometry (GC-MS, Thermo Fisher Scientific-TXQ Quantum XLS) and analyzed quantitatively by GC (Shimadzu, GC-2010 Plus) using an FID detector and a KB-WAX capillary column (Kromat Corporation, U.S.A.).

2.6. Computational methods

All the calculations were carried out by using density function theory (DFT) as implemented in the Vienna Ab initio Simulation Package (VASP). The Perdew, Burke, and Ernzerhof exchange and correlation functional with dispersion correction (PBE-D3) is used. The projector augmented wave (PAW) method has been used to describe inert core electrons. The cutoff energy of the plane-wave basis set is 400 eV. We relaxed the structures until the total energy changed within 1×10^{-4} eV per atom and the Hellmann–Feynman force on each atomic site was less than 0.05 eV/Å. Relaxed fcc bulk Ni was used for constructing a Ni (111) slab with three atomic layers and a vacuum space larger than 20 Å. The Gamma(Γ)-centered $2 \times 2 \times 1$ k-point grid was used for sampling reciprocal space with the Monkhorst-Pack method. In all the calculations, the top atomic layer of the surface was allowed to relax together with the molecule adsorbate, while the bottom two layers were kept fixed to present the bulk properties. The adsorption energy E_{ads} is given by the following equation:

$$E_{\text{ads}} = E_{\text{slab/ads}} - E_{\text{molecule}} - E_{\text{slab}},$$

where $E_{\text{slab/ads}}$ is the total energy of the catalyst surface adsorbed with molecules, E_{molecule} is the energy of an organic molecule in the free state, and E_{slab} is the energy of the metal surface slab employed.

3. Results and discussion

3.1. Synthesis and characterization of Ni@HCS catalyst

The Ni@HCS catalyst was synthesized through a vacuum-assisted impregnation method, as shown in Fig. 1a. First, the RF precursor (resorcinol formaldehyde resin) is coated on the SiO $_2$ sphere, and then the RF coat is carbonized at a high temperature. Subsequently, the inside SiO $_2$ is etched to form HCS. Then, Ni ions are introduced in the HCS by vacuum evaporation, a method that can encapsulate the metal ions on the void space of the HCS with the aid of a negative pressure environment. Finally, the sample was reduced to form the Ni@HCS catalyst.

The SEM results show that the spherical structure of the SiO $_2$ template is perfectly inherited by HCS (Fig. S1b). These spheres have a uniform size, and the diameter is approximately 250 nm (Fig. 1b). The TEM images of Fig. 1c demonstrate a hollow structure of those samples, indicating that the SiO $_2$ core had been successfully removed. The thickness of the HCS shell is about 15 nm for each HCS, which manifests that the RF precursor can grow evenly on the surface of the SiO $_2$ template. The Ni NPs are uniformly embedded into the void space of HCS, and the size is approximately 5–10 nm (Fig. 1d). The HRTEM image and the corresponding FFT image of the Ni NPs (Fig. 1e) reveal an inter-plane spacing of 0.206 nm corresponding to the Ni (111) crystal plane. The HADDF-STEM image and corresponding EDX mapping reveal the good distribution of Ni in the HCS (Fig. 1f).

Fig. 1g shows the nitrogen adsorption-desorption isotherm of Ni@HCS. From the pore size distribution, we can see that the sample is a mesoporous material, and the pore size is approximately 5–7 nm, which is smaller than the size of Ni nanoparticles, indicating that the Ni nanoparticles are difficult to separate from the catalysts during the reaction. Fig. 1h displays the XRD patterns of the Ni@HCS catalyst. The broad peak at about 23° can be attributed to the graphite carbon phase, which comes from the pyrolysis of the RF precursor. The diffraction peaks at approximately 44.5° and 52.3° can be attributed to the Ni (111) and Ni (200) crystal planes, respectively, showing an fcc crystal structure of metallic nickel (JCPDS NO. 01-1258). The surface chemical states of the catalysts were determined by XPS analysis. Fig. 1i shows the XPS survey spectra of Ni@HCS, which reveals the surface of the catalyst composed of C and Ni. It is worth mentioning that the surface Ni contents (1.15%) are far below the results determined by ICP-AES (15.42%) (Table S1), which reveals that the majority of Ni NPs are located inside the carbon shell and cavity of HCS. This result further confirms that this preparation method can encapsulate Ni species into the void space of HCS, which is in agreement with the TEM results. Fig. 1j shows the Ni 2p $_{3/2}$ spectra of the catalyst. The characteristic peaks at approximately 852.8 eV, 856.4 eV, and 861.9 eV can be ascribed to Ni 0 , Ni $^{2+}$, and Ni $^{2+}$ satellite peaks, respectively [9]. The oxidized Ni that exists on the external surface indicates that a handful of Ni deposited on the outside would be oxidized in the process of testing.

In summary, Ni species could be effectively introduced in the void space of HCS through negative pressure adsorption of vacuum-assisted impregnation, and highly dispersed Ni NPs could be uniformly constrained on the HCS in the Ni@HCS catalyst.

3.2. Catalytic performance of Ni@HCS

FAL is a vital bio-derived platform molecule that can be further employed as a building block for catalytic transformation into a series of important chemicals, such as FOL, THFOL, 2-MF, LA, CPO, and CPL. Here, AP-HRT of FAL into CPO (an important intermediate for synthesizing fungicides, pharmaceuticals, rubber, flavor, and other fragrance chemicals) was purposefully selected as the model reaction to evaluate the catalytic performance of the synthesized Ni@HCS catalyst.

FAL can selectively convert into different products depending on the catalysts, reaction medium, and reaction conditions (Fig. 2a). As a result, the influence of solvents on FAL conversion over the Ni@HCS

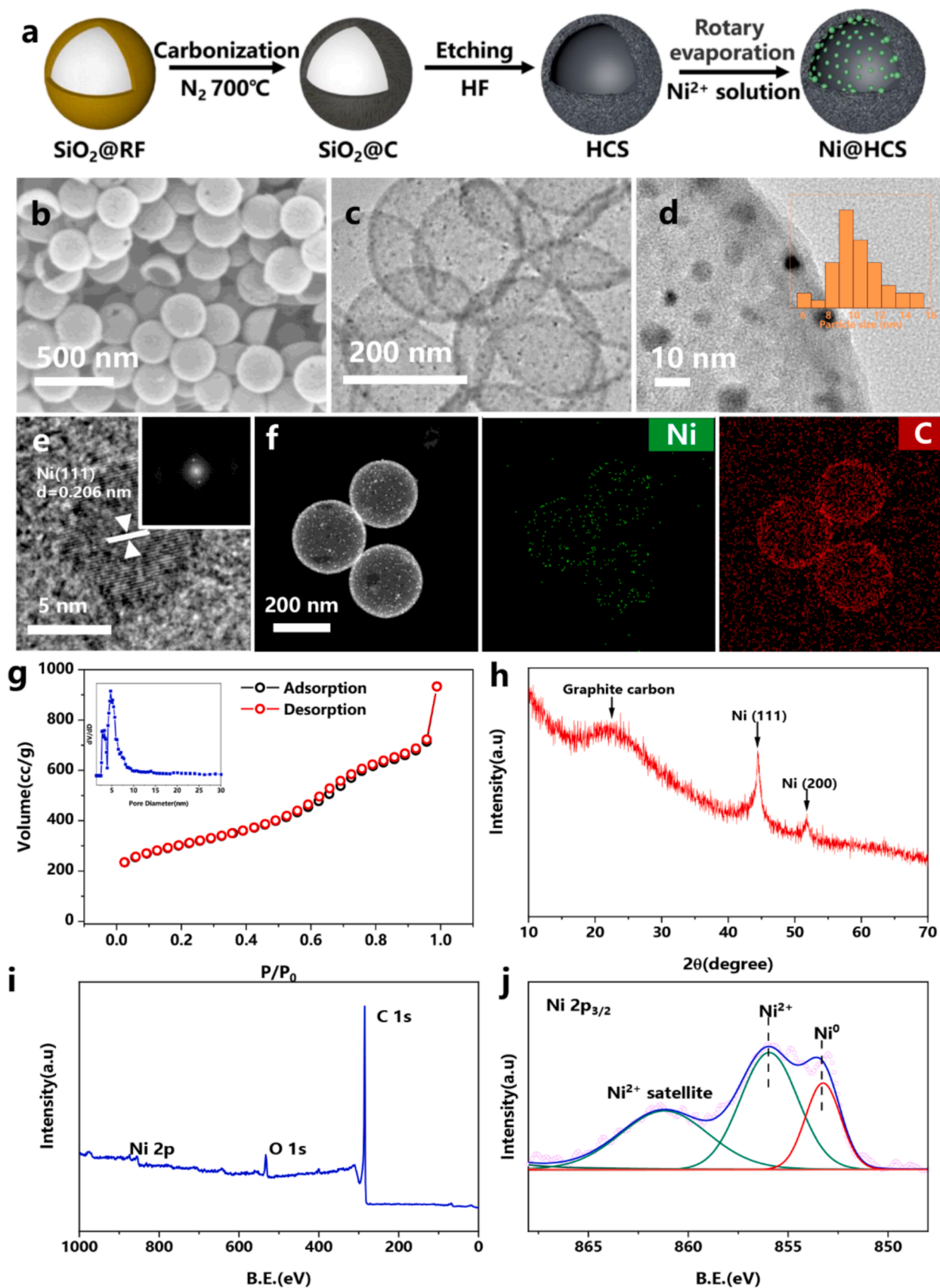


Fig. 1. (a) Illustration of the preparation process of Ni@HCS ; (b) SEM image of Ni@HCS ; (c) TEM image of Ni@HCS ; (d) HRTEM image of Ni@HCS ; (e) HRTEM image of a single Ni nanoparticle in Ni@HCS and corresponding fast Fourier transform (FFT) image; (f) HADDF-STEM image of Ni@HCS and corresponding EDX mapping; (g) Nitrogen adsorption-desorption isotherm and DFT pore size distributions of Ni@HCS ; (h) XRD pattern of Ni@HCS ; (i) XPS survey of Ni@HCS ; (j) $\text{Ni } 2p_{3/2}$ survey of Ni@HCS .

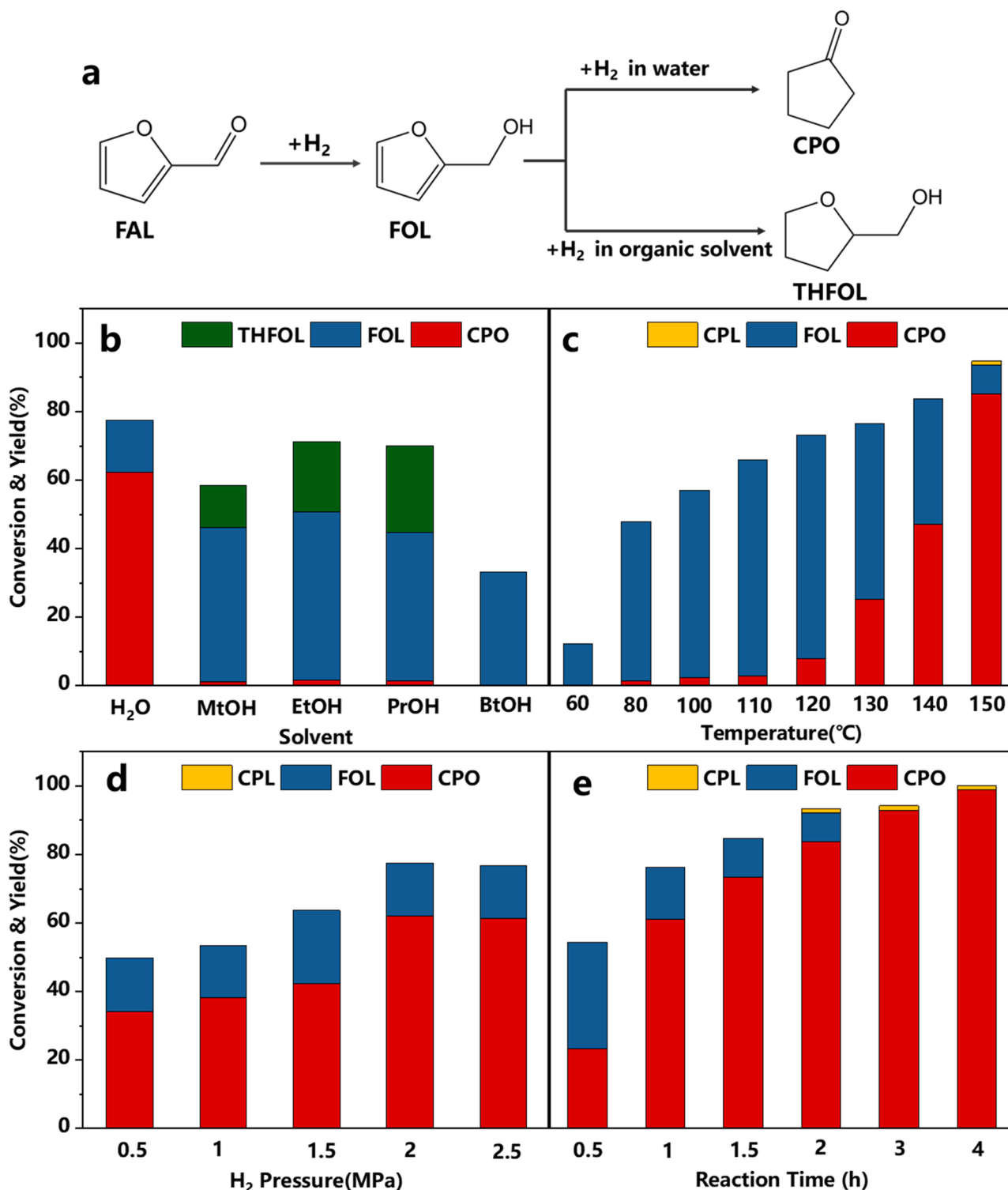


Fig. 2. (a) Different reaction process of FAL in water and organic solvent; catalytic performance of the Ni@HCS: (b) effect of solvent, 10 mg catalysts, 1 mmol FAL, 2 MPa H₂, 150 °C 10 ml solvent, 1 h; (c) effect of reaction temperature, 10 mg catalysts, 1 mmol FAL, 2 MPa H₂, 10 ml H₂O, 2 h; (d) effect of H₂ pressure, 10 mg catalysts, 1 mmol FAL, 150 °C, 10 ml H₂O, 1 h; (e) effect of reaction time, 10 mg catalysts, 1 mmol FAL, 2 MPa H₂, 150 °C, 10 ml H₂O.

catalyst was first investigated in water and compared with several organic alcohols. As shown in Fig. 2b, the activity and product distribution in water are completely outlined with the results in organic alcohols. The Ni@HCS catalyst demonstrates a higher activity in water than that of alcohols (water > EtOH ≈ PrOH > MtOH > BtOH). More importantly, the product distributions are completely different. When water was used as the reaction medium, FAL was converted into FOL and

CPO, and the main product was CPO (yield > 60%). THFOL will replace CPO as one of the products when an organic solvent is used. It is worth mentioning that a trace amount of CPO was also detected in the organic solvent. This could be attributed to a trace amount of water in the organic solvent (based on the purity of the organic reagent). Therefore, FAL would transform into CPO in water or THFOL in an organic reaction medium (as shown in Fig. 2a). Consequently, it could be concluded that

water as the reaction medium is an essential prerequisite for the catalytic conversion of FAL into CPO based on the results in Fig. 2b.

Fig. 2c shows the effect of reaction temperature on FAL conversion into CPO in the AP-HRT reaction. The Ni@HCS catalyst exhibits an initial activity (12.3% FAL conversion) at a low temperature of 60 °C, suggesting the characteristics of high catalytic activity in AP-HRT of FAL. In the range of 60–80 °C, the majority product is FOL, indicating that the carbonyl group in the FAL molecule could be activated and hydrogenated at a low reaction temperature. The FAL conversion increases obviously when the reaction temperature increases to 80 °C, showing a pleasing FAL conversion of 49.8%. Importantly, a small amount of CPO appears in the product at 80 °C, which is far lower than most of the reported initial reaction temperatures for the synthesis of CPO from FAL (Table S3). The conversion of FAL and yield of CPO gradually increase as the temperature further increases from 80 °C to 150 °C. FAL is almost completely converted at 150 °C, and the majority product is CPO with 87.8% yield. For further increasing the temperature, the yield of CPL gradually increases as the temperature is elevated to 180 °C. Then the CPL selectivity decreases for further increase the temperature to 200 °C. It could be attributed to the dynamic equilibrium between CPO hydrogenation and CPL dehydrogenation (Fig. S2). From the result of product distribution as a function of reaction temperature, it could be found that the CPO selectivity increases with decreasing FOL selectivity, suggesting that FOL could be further transformed into CPO by a rearrangement reaction under a higher reaction temperature. This indicates that not only hydrogenation of FAL takes place but also rearrangement of the generated FOL emerges in the range of 80–150 °C. A similar promotion effect could also be found based on H₂ pressure. As it turned from 0.5 MPa to 2 MPa, the FAL conversion and CPO selectivity were obviously promoted (Fig. 2d). There is little change as the H₂ pressure further increases, indicating that a H₂ pressure of 2 MPa is an optimal reaction condition. Fig. 2e shows the influence of reaction time on product distribution. Over half of the FAL (55.7% conversion) could be converted within 0.5 h of reaction at 150 °C. The yields of CPO and FOL are 25.1% and 30.6%, respectively. As the reaction proceeded, CPO gradually became the main product, and the selectivity of CPO reached 98.8% within 3 h of reaction. After 4 h of reaction, almost all of the furfural is converted, and the selectivity of CPO reaches 99.1%. Only a trace amount of by-production CPL is detected as the reaction proceeds. This suggests that FAL could be selectively transformed into CPO over the Ni@HCS catalyst via a hydrogenation-rearrangement tandem reaction at 150 °C and 2 MPa H₂.

3.3. Relationship of structure-to-activity for Ni@HCS

As described above, the Ni@HCS catalyst is a promising candidate that can transform FAL toward CPO with high selectivity in an AP-HRT reaction. To understand the relationship of the structure-to-activity of Ni@HCS in AP-HRT of FAL, the effects of the reduction temperature, shell thickness of HCS, and Ni loading amount on the structure and catalytic performance are deeply investigated.

3.3.1. Effect of reduction temperature

To investigate the effect of the reduction temperature of the Ni@HCS catalyst, TPR analysis was first implemented to understand the reduction behavior of the catalyst at different reduction temperatures. As shown in Fig. 3a, the TPR profile of Ni@HCS shows three characteristic peaks at about 245 °C, 300 °C, and 430 °C. Considering the results of TEM-EDS and ICP, no other element was detected that could be reduced by H₂ except Ni ions. The three peaks could be related to the reduction of a small amount of Ni species that interacted weakly with HCS (Ni clusters and small particles on the outer surface of the carbon shell), the small Ni interacted strongly with the support (the Ni species in the pore channel interacting with carbon) and the Ni nanoparticles interacted strongly with HCS (Ni species in the cavity interacting with carbon) [30]. The intensity of the peak related to the weakly interacting Ni was far weaker than that of the other two types, indicating that most of the Ni was encapsulated into the cavity of HCS. In light of the information supplied by the TPR result, the catalysts are reduced at 250 °C, 300 °C, 450 °C to obtain samples with different reduction temperatures to measure their catalytic performances. It can be clearly seen from Fig. 3b that these three samples possess a huge catalytic capacity gap. The catalyst reduced at 450 °C affords nearly 80% FAL conversion and 60% CPO yield after 1 h of reaction at 150 °C. However, the other two samples (reduced at 250 °C and 300 °C) only convert less than 30% FAL under the same conditions and almost all of FAL is converted into FOL (> 99.9% selectivity). The above results suggested that 450 °C is a suitable reduction temperature for the production of CPO from FAL.

3.3.2. Effect of carbon shell

From the synthesis schematic diagram in Fig. 1a, it can be seen that the thickness of the HCS is highly related to the phenolic resin deposited on the outside of SiO₂, and the formation of phenolic resin is determined by the amount of resorcinol and formaldehyde added during preparation. In this work, the amount of resorcinol was adjusted to 0.2 g, 0.4 g

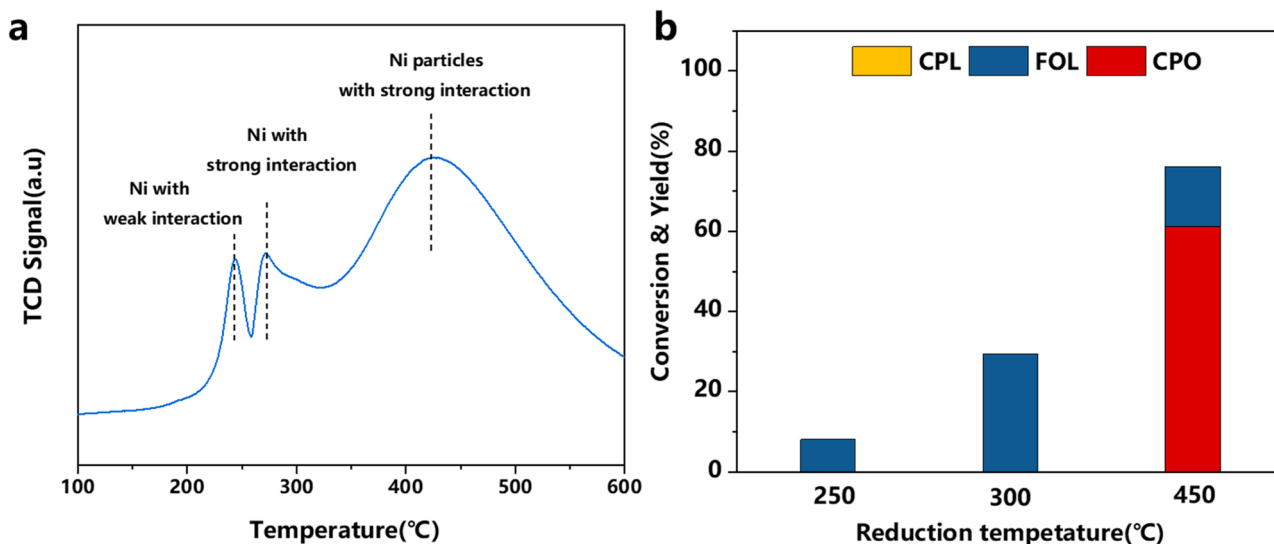


Fig. 3. (a) TPR profile of Ni@HCS. Three peaks represent different forms of Ni species interacting with HCS; (b) the effect of reduction temperature on the catalytic activity. Reaction conditions: 10 mg catalysts, 1 mmol FAL, 2 MPa H₂, 10 ml H₂O, 150 °C, 1 h.

0.6 g, and 0.8 g (the dosage of formaldehyde was changed to the corresponding level) to get HCS with shell thicknesses of 5 nm, 15 nm, 25 nm, and 35 nm, respectively. The SEM image shows that HCS with a 5 nm shell thickness is unable to maintain the spherical structure because of serious collapse and breakage, which would have a great influence on subsequent metal loading and catalytic experiments (Fig. S1a). For the 15 nm, 25 nm, and 35 nm shell thicknesses of HCS, the spherical structure is maintained perfectly. Correspondingly, a series of Ni@HCS catalysts were derived after Ni NPs were deposited on HCS with different shell thicknesses. As shown in Fig. 1b–f and Fig. S3, the Ni NPs disperse and encapsulate uniformly on the pore structure and cavity of HCS for all of the Ni@HCS catalysts. N₂-physical adsorption experiments were carried out to determine the specific surface areas and pore distributions. As shown in Fig. 1g, Fig. S4, and Table S1, all of these Ni@HCS samples possess large specific surface areas. Ni@HCS with the thinnest shell shows the largest surface area of 867.8 m² g^{−1} among the three samples, which can afford a large number of active sites for adsorption and activation of reactants.

The XRD patterns of the three samples (Fig. 4a) show similar characteristic peaks, which can be attributed to metallic Ni. The intensity of the diffraction peak apparently increases with the shell thickness, indicating the formation of larger crystal particles. This phenomenon can be attributed to the decrease of the overall number of carbon spheres in a unit mass with the increase of HCS shell thickness, which means that the overall number of carbon spheres in Ni@HCS samples following the shell thickness order of 15 nm > 25 nm > 35 nm. Therefore, the Ni NPs are more dispersed in the Ni@HCS with a thinner shell. In other words, the overall number of individual nanoreactors in the Ni@HCS catalyst with the thinnest shell is far larger than its counterparts. It can not only prevent Ni NPs from sintering and agglomerating but also contribute to more active sites. The XPS analysis of these catalysts (Fig. S5) shows similar results, and the surface Ni ratio of Ni@HCS with a thicker shell determined by XPS is far below the results from ICP-AES (Table S1, S2). The Ni NPs mainly existed in the pore structure and cavity of HCS, which is in agreement with the TEM images (Fig. S3). This further proves that the void space of HCS would be the reaction zone in the Ni@HCS catalyst and can be treated as an individual nanoreactor. As a result, all of the Ni@HCS catalysts display fine CPO selectivity in the reaction; among them, Ni@HCS with the thinnest shell demonstrates the optimal catalytic performance (Fig. 4b) with the highest FAL conversion and CPO yield compared with Ni@HCS with a thicker shell. A heterogeneous reaction contains the process of mass transfer and diffusion of reactants, adsorption of the reactants on the liquid-solid interface, diffusion of

reactants from the interface to the active sites, and surface reaction. For the Ni@HCS catalyst, the active Ni NPs are mainly encapsulated inside the cavity of HCS. In the reaction, the reactant of FAL should pass through the carbon shell to contact active Ni NPs. The shell thickness would greatly influence the mass transfer of the reactant. Therefore, the mass transfer rate could be greatly limited as the carbon shell thickness increases, which would also have a negative effect on the contact between the reactant and catalyst to reduce catalytic reaction efficiency. Therefore, if not specified, the Ni@HCS catalyst mentioned in this article refers specifically to the sample with a shell thickness of 15 nm.

Ni@HCS with a small cavity size (approximately 100 nm) and large cavity size (approximately 400–500 nm) were also synthesized by adjusting the amount of TEOS and ammonia in the synthesis process to investigate the influence of cavity size. The SEM and TEM images show that the Ni NPs are also successfully loaded into the cavity of these two catalysts (Fig. S6). The XRD patterns of these samples show similar characteristic peaks as Ni@HCS with a middle size (200 nm) that was mentioned above (Fig. 5a). However, the intensity of Ni increased with increasing cavity size, indicating the sintering and growth of Ni particles. Although the Ni content of these catalysts is controlled at the same level, the larger cavity can encapsulate more Ni species and give more opportunities to form large size of NPs. As a result, Ni@HCS with the largest cavity size shows the worst catalytic activity in the reaction (Fig. 5b). In contrast, Ni@HCS with a small cavity size shows more dispersed Ni NPs and still displays poorer catalytic activity than Ni@HCS with a middle cavity size. This phenomenon can be related to the mass transfer rate, as the small cavity would greatly limit reactant diffusion during the reaction, thus displaying poorer activity than the catalyst with the middle cavity size [24]. Therefore, the Ni@HCS with middle size cavity (200 nm) displays the optimal catalytic performance in the AP-HRT reaction. Therefore, if not specified, the Ni@HCS catalyst mentioned in this article refers specifically to the sample with a cavity size of 200 nm.

3.3.3. Effect of Ni loading

Ni@HCS catalysts with different Ni loadings were also prepared. The ICP-AES results (Table S2) show that the Ni loading of all catalysts matches expectations, suggesting a controllable loading of Ni content. The TEM image (Fig. S7) shows that when the Ni content was below 10 wt%, the Ni NPs were sparsely distributed in HCS. For the 15 wt% Ni loading, the Ni NPs disperse and encapsulate uniformly in the Ni@HCS catalyst. However, when the Ni content reaches 25 wt%, sintering and agglomeration of Ni NPs emerge obviously and aggravate gradually with

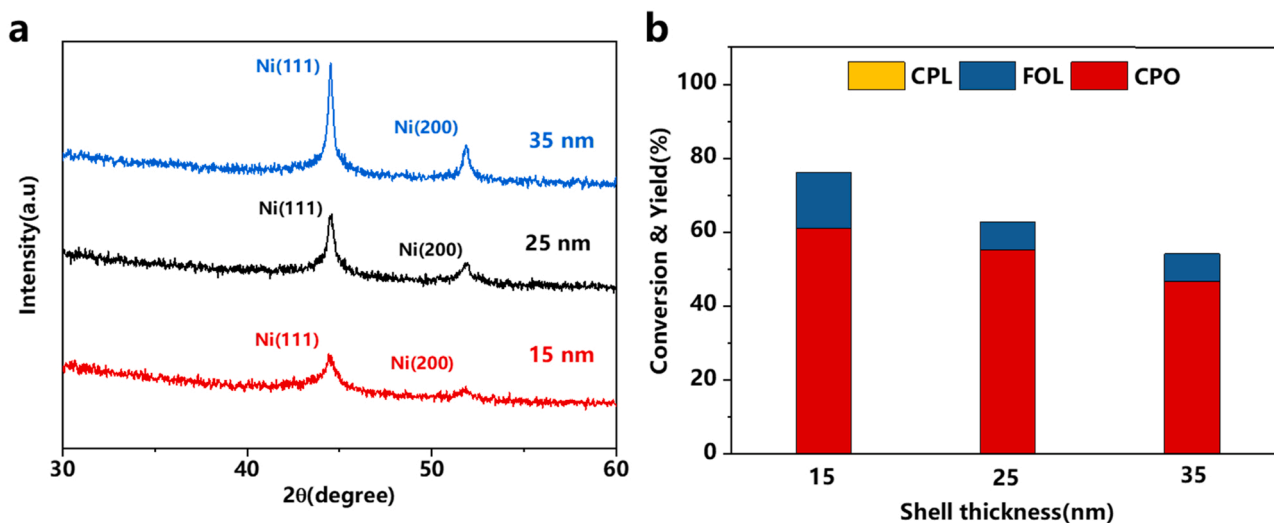


Fig. 4. (a) XRD patterns of Ni@HCS with different carbon thicknesses; (b) effect of the shell thickness on the catalytic activity. Reaction conditions: 10 mg catalysts, 1 mmol FAL, 2 MPa H₂, 10 ml H₂O, 150 °C, 1 h.

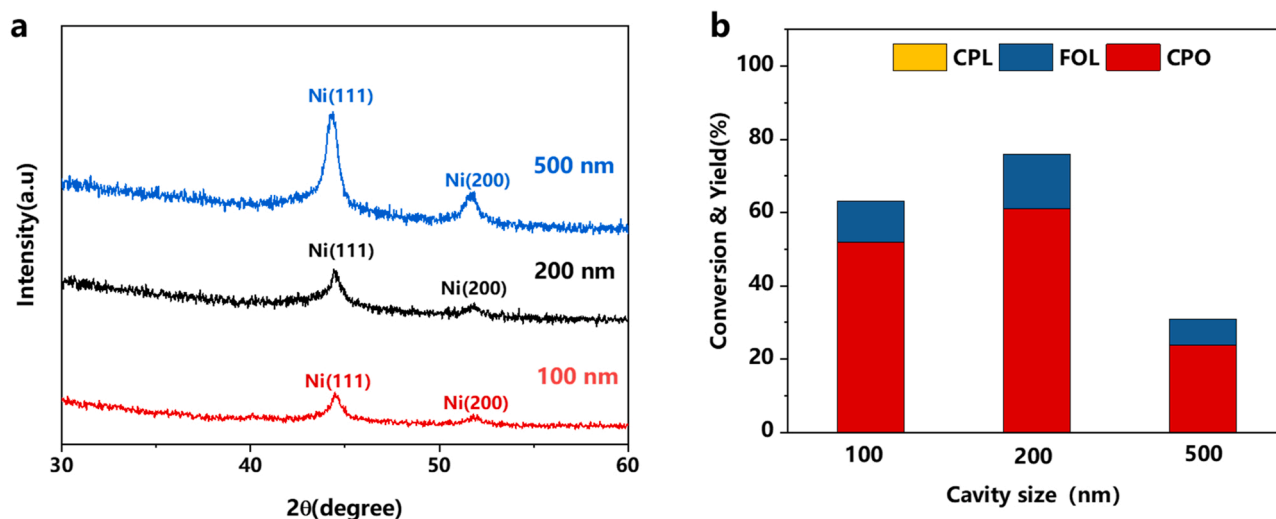


Fig. 5. (a) XRD patterns of Ni@HCS with different cavity sizes; (b) effect of the cavity size on the catalytic activity. Reaction conditions: 10 mg catalysts, 1 mmol FAL, 2 MPa H_2 , 10 ml H_2O , 150 °C, 1 h.

a further increase in Ni content. The XRD patterns (Fig. 6a) can further confirm the results of the TEM image as the intensity of Ni@HCS increases obviously with Ni content, confirming serious agglomeration at a high Ni loading. Fig. 6b shows the effect of Ni content on the catalytic performance in AP-HRT of FAL. The FAL conversion has a great enhancement as the Ni content raises from 10% to 15%, which can be attributed to the increase in active sites. Although the FAL conversion and the yield of CPO can be maintained at a stable level to further increase the Ni content from 15 wt% to 35 wt%, the TOF value shows that Ni@HCS with 15 wt% Ni gives the highest catalytic efficiency. The FAL conversion and CPO yield drop drastically as the Ni content further increases to 45 wt%. The corresponding TEM and XRD results show very serious aggregation and sintering of Ni NPs. As a result, the Ni content should be adjusted to 15 wt% to get the most satisfactory catalytic results and efficiency. Hence, if not specified, the Ni content in the Ni@HCS catalyst referred to in this work is 15 wt%.

3.4. Void-confinement effect and amplification tests of the Ni@HCS catalyst

As studied, the synthesized Ni@HCS catalyst demonstrates high activity and excellent selectivity for converting FAL into CPO. The

motivation for the high catalytic performance should be further explored for the Ni@HCS catalyst. As known, the reaction behavior highly relies on the active metal loading zone (exterior surface, pore channel, or cavity) for hollow structure nanomaterial supported metal catalysts. For active metal loading in pore and void spaces, a void-confinement effect emerges as one of the most fundamental and prerequisite effects for either obviously enhancing the catalytic activity or tuning selectivity in heterogeneous catalysis (Fig. 7a).

Herein, the void-confinement effect of the Ni@HCS catalyst was also investigated in the FAL AP-HRT reaction and compared with that of a non-hollow Ni catalyst (Ni/AC, an active carbon-supported Ni catalyst obtained via the precipitation method; the XRD pattern is shown in Fig. S8). The Ni content was controlled under the same conditions, which was proven by ICP-AES (Table S2). In contrast, the active Ni species are mainly deposited on the external surface of the support in the Ni/AC catalyst, which is different from the Ni@HCS catalyst (Ni species are mainly encapsulated in the void space of HCS). There were huge differences in catalytic performance over the Ni@HCS (Fig. 7b) and Ni/AC catalysts (Fig. 7c). In the first run of catalytic tests, Ni/AC shows poor activity with 56.2% FAL conversion after a 2 h reaction at 150 °C (Fig. 7c). In addition, a broad product distribution composed of FOL, CPO, THFOL, and 2-MF was detected for the Ni/AC catalyst, and the

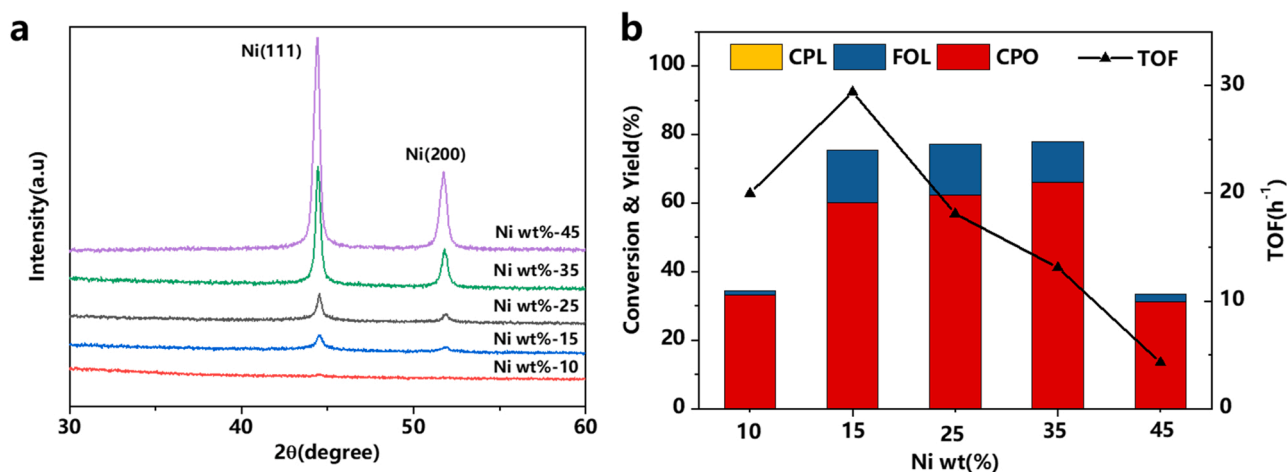


Fig. 6. (a) XRD patterns of Ni@HCS with different Ni loadings; (b) effect of Ni loading on the catalytic activity. Reaction conditions: 10 mg catalysts, 1 mmol FAL, 2 MPa H_2 , 10 ml H_2O , 150 °C, 1 h.

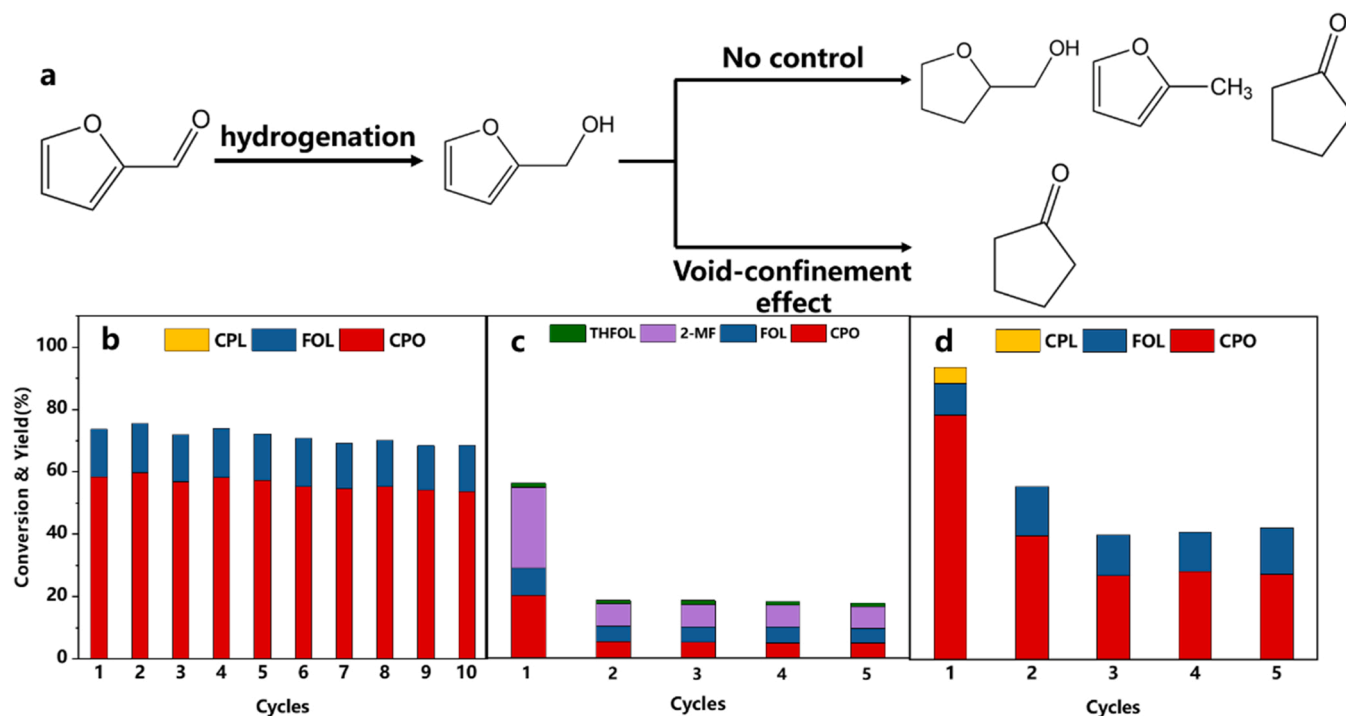


Fig. 7. Effect of the void-confinement of HCS: (a) Illustration of the different paths under the void-confinement effect; (b) cycle experiments of Ni@HCS; (c) cycle experiments of Ni/AC; (d) cycle experiments of Ni@AC.

selectivity of CPO was only 40.3%. Meanwhile, under the same reaction conditions, the Ni@HCS catalyst displays a far higher FAL conversion with the product composition of CPO and FOL, and the CPO selectivity is 85.3%. More importantly, with prolonged reaction, the CPO selectivity reached 99.1% after 3 h of reaction (Fig. 2e). From these results, it could be found that FAL could selectively transform into CPO for active Ni species deposited in the void space (Ni@HCS) but would randomly convert into diverse products (THFOL, FOL, CPO, 2-MF, etc.) for active Ni species loading at the external surface (Ni/AC), as shown in Fig. 7a.

The high and specific selectivity of Ni@HCS could be ascribed to the shape-selective catalysis induced by the void-confinement effects rooted in the hollow structures of HCS, similar to molecular-sieving shape-selective catalysis [31,32]. To further prove the void-confinement effect, another AC-supported Ni catalyst (Ni/AC) was also synthesized through a vacuum-assisted impregnation method, similar to the preparation of Ni@HCS. With the assistance of vacuum impregnation, the Ni NPs are mainly deposited into the micropore channel of AC, thus forming a molecular-sieving like void space. As expected, Ni/AC also shows a similar reaction behavior to the Ni@HCS catalyst (Fig. 7b and d) in the first run of the catalytic experiment due to the void effect of the Ni/AC catalyst. However, the Ni@HCS catalyst demonstrates excellent catalytic stability, which is far superior to the Ni/AC and Ni@AC catalysts. Ni@HCS maintains its activity after 10 cycles of use, and the Ni content slightly decreases after 10 cycles of testing, which could be attributed to the loss of a small amount of Ni species deposited on the outer surface of HCS with weak interaction. The TEM image and XRD pattern of the used Ni@HCS also have no obvious change (Figs. S9, 10), showing the superb stability of Ni@HCS due to the protective effect of the HCS shell under harsh conditions. However, for the used Ni/AC, the Ni content drops to 5.5 wt% (based on the ICP-AES result) due to the serious leaching effect under high temperature and pressure aqueous-phase hydrothermal reaction conditions. Even for the Ni species deposited at the pore channel in the Ni@AC catalyst, it also displays a serious leaching phenomenon, and the Ni content decreases from 14.9 wt% to 6.0 wt% after the reaction, similar to the Ni/AC catalyst.

Combined with the previous literature [23,27] and our experimental

data, the good selectivity of Ni@HCS can be related to the shape-selective catalysis induced by the void-confinement effect of the HCS void-space structure. The dispersing effect of Ni NPs by HCS leads to the formation of abundant individual nanoreactors, which greatly improve the activity of the Ni@HCS catalyst. The HCS shell can effectively prevent the active Ni species from sintering, leaching, and aggregating, thus greatly improving the durability of the catalyst, even under harsh reaction conditions. Therefore, the Ni@HCS catalyst exhibits high activity, excellent selectivity, and outstanding stability in the AP-HRT reaction of FAL into CPO.

In view of the excellent catalytic stability, the amplification capability of the Ni@HCS catalyst was also investigated in a gram-scale test (FAL 1.92 g, catalyst 100 mg, H₂O 100 ml). As shown in Fig. 8, the reaction rate was fast at the initial stage, as the conversion of FAL reached

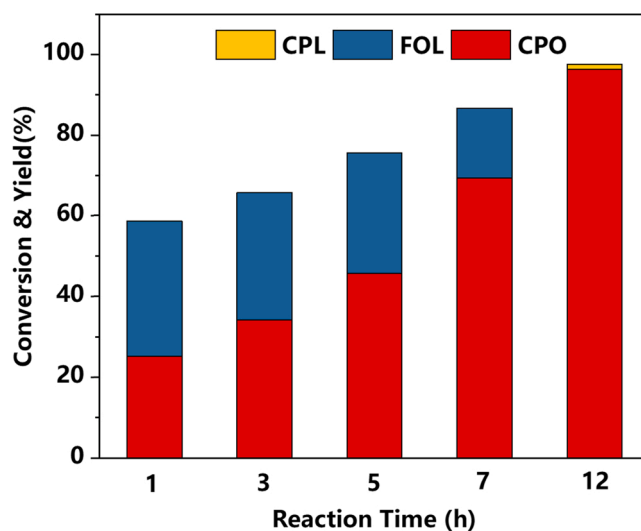


Fig. 8. Large-scale experiment of Ni@HCS. Reaction conditions: 100 mg catalysts, 20 mmol FAL, 2 MPa H₂, 100 ml H₂O, 150 °C.

nearly 60% within only 1 h of reaction. This could be attributed to the exothermic characteristics of hydrogenation resulting in the instantaneous reaction temperature of the active surface being far higher than that of setting the temperature at the initial reaction stage. The reaction rate drops down to a smooth level after the first one-hour reaction, and the conversion of FAL gradually increases with prolonged reaction time. The yield of CPO increases following the decrease in FOL yield, which suggests that the generated FOL gradually converts into CPO. After 12 h of reaction, the full conversion of FAL was accomplished, and the yield of CPO was as high as 96.2%, close to the small-scale experiment (Fig. 2e). The results manifest the good amplification capability of Ni@HCS, which has the potential for industrial application.

3.5. Reaction process and kinetics

As mentioned, the catalytic routes and product distribution of FAL hydrogenation over the Ni@HCS catalyst are quite different in water and organic solvents. FAL is more likely to form CPO in an aqueous phase but to generate THFOL in organic alcohol. To thoroughly investigate this issue, water and ethanol mixing solvents were employed in the reaction, and the effect of the water to ethanol ($\text{H}_2\text{O}/\text{EtOH}$) volume ratio was carefully investigated, as shown in Fig. S11. At a low water content ($\text{H}_2\text{O}/\text{EtOH}$ volume ratio of 1/9), FOL and THFOL are the main products with only a trace amount of CPO generation. The yield of THFOL gradually decreased with increasing CPO yield as the water content increased from 1/9–7/3. When the $\text{H}_2\text{O}/\text{EtOH}$ volume ratio is 9/1, CPO is the main product, but the generation of THFOL disappears.

When we look back at the molecular structure of FAL and CPO, one finding is that only hydrogenation is inadequate to transform FAL toward CPO. FAL should pass through hydrogenation of the unsaturated $\text{C}=\text{C}$ bonds in the furan ring, removal of the oxygen in the furan ring and reconstruction of the $\text{C}=\text{O}$ bond in the side chain of the five-carbon ring. Correspondingly, it should undergo hydrogenation and rearrangement tandem reactions to transform FAL toward CPO. In the rearrangement reaction, water is an indispensable reactant to rebuild the $\text{C}=\text{O}$ in the side chain. Therefore, water is the optimal solvent and reactant for the highly selective transformation of FAL into CPO. More importantly, from the FAL conversion and FOL yield, it could be concluded that water can also effectively enhance FAL and FOL transformation. This indicates that water in the FAL AP-HRT reaction not only acts as a reactant but also provides an environment that is beneficial to the route toward CPO generation.

The overall process for transforming FAL toward CPO includes a sequence of reactions and intermediates. To understand the process in detail, a series of kinetic experiments were carefully carried out. In the FAL AP-HRT reaction, the reactants are FAL, hydrogen, and water. The amounts of hydrogen and water are excessive and thus can be regarded as a constant during the kinetic experiments. The reaction rate would be highly correlated with the concentration of FAL or FOL. As a result, we used FAL and FOL as substrates to study the reaction dynamics of FAL hydrogenation to FOL and FOL rearrangement to CPO. To obtain the intrinsic reaction rate, the conversion of reactant is controlled at a low level. Fig. S12 shows the reactant conversion and product yield as a function of reaction time at the different reaction temperatures. On these

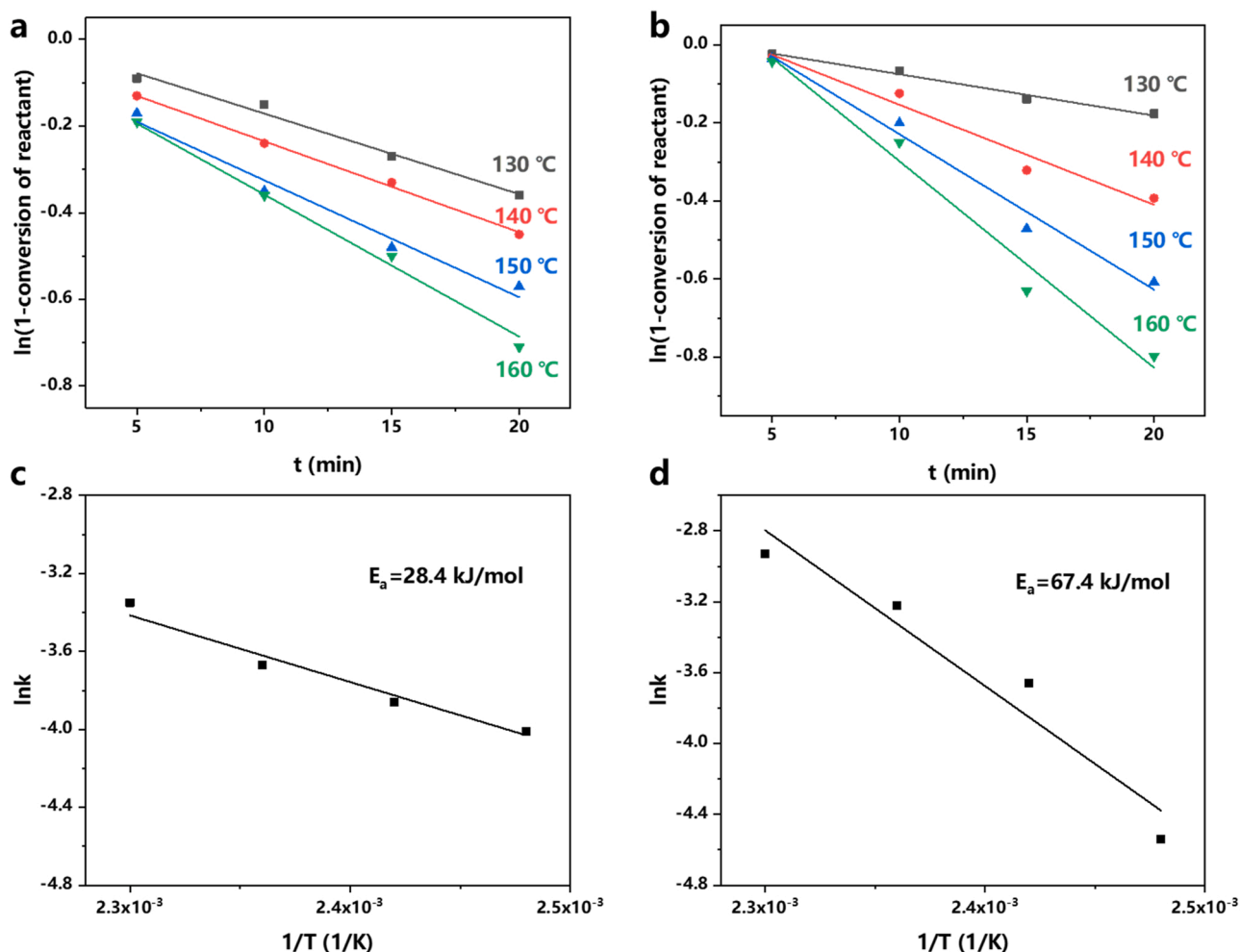


Fig. 9. Kinetic profile of (a) FAL hydrogenation and (b) FOL rearrangement; Arrhenius plots for (c) FAL hydrogenation and (d) FOL rearrangement.

bases, the two catalytic systems exhibit first-order reaction kinetic behaviors from 130 °C to 160 °C, as shown in a linear relation between the Napierian logarithm of conversion ($\ln(1-\text{conversion of reactant})$) and reaction time (Fig. 9). The slope of the linear curve is the reaction rate constant k (min^{-1}). The reaction rate constants of FAL hydrogenation and FOL rearrangement are calculated and listed in Table 1.

Table 1 shows that below 140 °C, the rate of FOL rearrangement (0.010 min^{-1}) is lower than that of FAL hydrogenation (0.018 min^{-1}), suggesting that FOL rearrangement is the rate control step of this tandem reaction. Above 140 °C, the rate of FOL rearrangement increased rapidly, and FAL hydrogenation became the rate control step of this reaction. The reaction activation energy (E_a) was further calculated based on the Arrhenius equation ($\ln k = -E_a/RT + C$), and the values are listed in Table 1. The reaction of FAL hydrogenation shows a lower E_a value (28.4 kJ/mol) than the FOL rearrangement (67.4 kJ/mol), suggesting that FOL rearrangement is harder to occur than FAL hydrogenation, which is in accordance with other experimental results. It can also be interpreted that 2-CPONE (2-cyclopenten-1-one), which had not been detected in previous experiments (Fig. 2), was detected in a short reaction time in the kinetic experiments (Fig. S13a). 2-CPONE is rapidly converted to cyclopentanone (Fig. S13b), which is an important intermediate in the rearrangement process.

As important immediate 2-CPONE was detected in the reaction (Fig. S13a), the overall process of the FAL AP-HRT reaction can be presumed to be in accordance with the above results, and the corresponding DFT calculation was applied to determine the most likely reaction route (Fig. 10, Table S4). The adsorption energy of FAL on the Ni (111) crystal plane was first calculated. With flat and perpendicular adsorption configurations, the adsorption energies are -1.805 eV and -0.811 eV , respectively, which suggests that FAL prefers to adsorb on the Ni (111) surface as a flat configuration. Then, the adsorption energies of subsequent products were calculated, and it was found that all of them have strong adsorption on Ni. The hydrogenation of FAL with 2 H^* (active hydrogen derived from H_2 dissociation) can result in the formation of FOL, and the calculated reaction energy was -0.085 eV . The $-\text{OH}$ in FOL could easily interact with one H^* and take off as one H_2O molecule, forming the intermediate product $\text{C}_5\text{H}_5\text{O}$. The reaction from FOL to $\text{C}_5\text{H}_5\text{O}$ is an exothermic process with an energy release of 1.045 eV , which can benefit the following rearranging and restructuring processes. For $\text{C}_5\text{H}_5\text{O}$ to HCP (3-hydroxy-cyclopentanone), an energy input of 0.386 eV is needed, and this process requires the participation of water, which can explain why the reaction toward CPO is preferable in water. HCP is unstable and could be further dehydrated to obtain the intermediate 2-CPONE (reaction energy -0.783 eV), and 2-CPONE is rapidly hydrogenated to produce CPO (reaction energy -0.802 eV). Although the reaction energy of CPO to CPL is only -1.124 eV , the reaction hardly takes place in this work, as shown in the catalytic tests (Fig. 2), suggesting that the reaction of CPO to CPL is not only thermodynamically controlled but also kinetically controlled. From the above results, it could be speculated that the active surface of Ni (111) in the Ni@HCS catalyst can exhibit superior catalytic performance in the FAL AP-HRT reaction.

3.6. Versatility of Ni@HCS catalyst in AP-HRT reaction

The versatility of the Ni@HCS catalyst was also studied by applying it in the AP-HRT reaction of different bio-derived furan derivatives

Table 1
Some results of the kinetic experiments.

Reactions	k (min^{-1})				E_a (kJ/mol)
	130 °C	140 °C	150 °C	160 °C	
FAL hydrogenation	0.018	0.021	0.027	0.033	28.4
FOL rearrangement	0.010	0.026	0.039	0.053	67.4

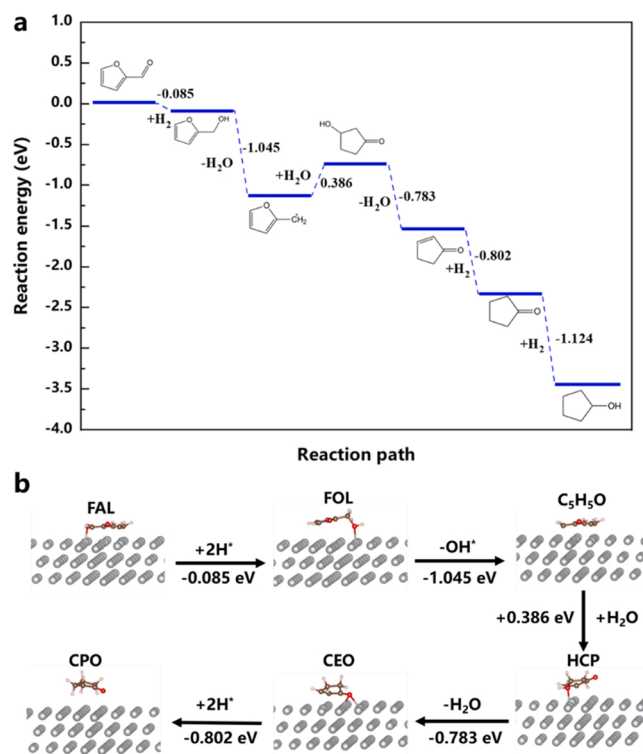
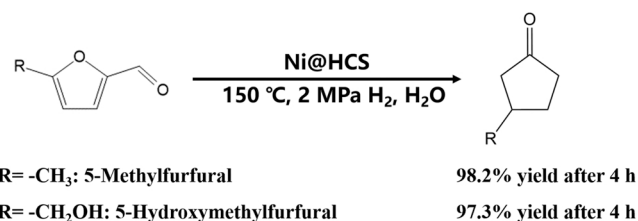


Fig. 10. (a) Reaction path of FAL to CPL; (b) adsorption configuration in different reaction processes.



Scheme 1. Catalytic performance of Ni@HCS in other types of furaldehyde. Conditions: 10 mg catalysts, 1 mmol reactant, 2 MPa H_2 , 10 ml H_2O , 150 °C, 4 h.

(Scheme 1). When 5-methylfurfural is the substrate, the main product is 3-methyl-cyclopentanone, and the yield could reach 98.2% within a 4 h reaction at 150 °C. When the functional group (R) in the reactant changes from methyl to methoxy, the corresponding product also changes to 3-methoxy-cyclopentanone, and the yield can also be maintained above 95%. These results confirm the universality of the Ni@HCS catalyst in the AP-HRT reaction of bio-derived furan derivatives to the corresponding cyclopentanone derivatives. More importantly, this method is still applicable when producing such a nanoreactor with other active metals for different reactions, showing the universality of this method (Fig. S14).

4. Conclusion

In this work, the Ni@HCS nanoreactor was constructed through a vacuum-assisted impregnation method. The catalyst displays superior activity, selectivity, and stability in the AP-HRT reaction of FAL toward CPO. The high activity stems from the dispersing effect of Ni NPs by HCS to form abundant individual nanoreactors. The good selectivity of Ni@HCS could be attributed to the shape-selective catalysis induced by the void-confinement effect of the HCS. The excellent stability originates from the protective effect of the HCS shell against active Ni NP sintering,

leaching, and aggregation. The DFT calculation combined with experimental results confirms the vital role of water on the active sites in the AP-HRT reaction, which plays a key role in the rearrangement of intermediate FOL into CPO. The present work can help us understand the void-confinement effect of a non-noble metal hollow catalyst in the aqueous-phase tandem reaction and how the hollow structure tunes the catalytic performance in shape-selective catalysis.

CRedit authorship contribution statement

Zhi Hu: Investigation, Formal analysis, Visualization, Writing – original draft. **Miaomiao Han:** Calculation, data analysis. **Chun Chen:** Conceptualization, Methodology, Validation, Formal analysis, Writing – review & editing, Funding acquisition. **Zidan Zou:** Investigation, Formal analysis. **Yue Shen:** Writing – review & editing. **Zhen Fu:** ICP analysis. **Xiaoguang Zhu:** Formal analysis. **Yunxia Zhang:** Methodology, Validation. **Haimin Zhang:** Conceptualization, Investigation, Formal analysis. **Huijun Zhao:** Resources, Investigation. **Guozhong Wang:** Supervision, Project administration.

Declaration of Competing Interest

There are no conflicts to declare.

Acknowledgments

This work was supported by the National Natural Science Foundation of China (Grant No. 51871209, No. 52072371), Key Technologies Research and Development Program of Anhui Province (202004a06020056), and Instrument Developing Project of the Chinese Academy of Sciences (yz201421). We thank the Hefei advanced computing center for theoretical calculations.

Author contributions

These authors contributed equally: Z. Hu and M.M. Han. The manuscript was written through contributions of all authors. All authors have given approval to the final version of the manuscript.

Appendix A. Supporting information

Supplementary data associated with this article can be found in the online version at [doi:10.1016/j.apcatb.2022.121140](https://doi.org/10.1016/j.apcatb.2022.121140).

References

- [1] G. Nie, H. Wang, Q. Li, L. Pan, Y. Liu, Z. Song, X. Zhang, J.-J. Zou, S. Yu, Co-conversion of lignocellulosic derivatives to jet fuel blending by an efficient hydrophobic acid resin, *Appl. Catal. B-Environ.* 292 (2021), 120181, <https://doi.org/10.1016/j.apcatb.2021.120181>.
- [2] A. Bohre, M.I. Alam, K. Avasthi, F. Ruiz-Zepeda, B. Likozar, Low temperature transformation of lignocellulose derived bioinspired molecules to aviation fuel precursor over magnesium–lanthanum mixed oxide catalyst, *Appl. Catal. B-Environ.* 276 (2020), 119069, <https://doi.org/10.1016/j.apcatb.2020.119069>.
- [3] J. Wu, G. Gao, J. Li, P. Sun, X. Long, F. Li, Efficient and versatile CuNi alloy nanocatalysts for the highly selective hydrogenation of furfural, *Appl. Catal. B-Environ.* 203 (2017) 227–236, <https://doi.org/10.1016/j.apcatb.2016.10.038>.
- [4] W. Yao, J. Chen, Y. Wang, R. Fang, Z. Qin, X. Yang, L. Chen, Y. Li, Nitrogen-doped carbon composites with ordered macropores and hollow walls, *Angew. Chem. Int. Ed.* 60 (2021) 2–8, <https://doi.org/10.1002/anie.202108396>.
- [5] P. Zhou, Y. Chen, P. Luan, X. Zhang, Z. Yuan, S.-X. Guo, Q. Gu, B. Johannessen, M. Mollah, A.L. Chaffee, D.R. Turner, J. Zhang, Selective electrochemical hydrogenation of furfural to 2-methylfuran over a single atom Cu catalyst under mild pH conditions, *Green Chem.* 23 (2021) 3028–3038, <https://doi.org/10.1039/d0gc03999c>.
- [6] P. Cao, L. Lin, H. Qi, R. Chen, Z. Wu, N. Li, T. Zhang, W. Luo, Zeolite-encapsulated Cu nanoparticles for the selective hydrogenation of furfural to furfuryl alcohol, *ACS Catal.* 11 (2021) 10246–10256, <https://doi.org/10.1021/acscatal.1c02658>.
- [7] W. Gong, C. Chen, H. Zhang, G. Wang, H. Zhao, In situ synthesis of highly dispersed Cu–Co bimetallic nanoparticles for tandem hydrogenation/rearrangement of bio-derived Furfural in aqueous-phase, *ACS Sustain. Chem. Eng.* 6 (2018) 14919–14925, <https://doi.org/10.1021/acssuschemeng.8b03418>.
- [8] X. Li, Q. Deng, S. Zhou, J. Zou, J. Wang, R. Wang, Z. Zeng, S. Deng, Double-metal cyanide-supported Pd catalysts for highly efficient hydrogenative ring-rearrangement of biomass-derived furanic aldehydes to cyclopentanone compounds, *J. Catal.* 378 (2019) 201–208, <https://doi.org/10.1016/j.jcat.2019.08.036>.
- [9] S. Chen, T.T. Qian, L.L. Ling, W. Zhang, B.B. Gong, H. Jiang, Hydrogenation of furfural to cyclopentanone under mild conditions by a structure-optimized Ni–NiO/TiO₂ heterojunction catalyst, *ChemSusChem* 13 (2020) 5507–5515, <https://doi.org/10.1002/cssc.202001424>.
- [10] R. Ma, X.-P. Wu, T. Tong, Z.-J. Shao, Y. Wang, X. Liu, Q. Xia, X.-Q. Gong, The critical role of water in the ring opening of furfural alcohol to 1,2-pentanediol, *ACS Catal.* 7 (2016) 333–337, <https://doi.org/10.1021/acscatal.6b02845>.
- [11] M.K. Stones, E.M.J. Banz Chung, I.T. da Cunha, R.J. Sullivan, P. Soltanipannah, M. Magee, G.J. Umphrey, C.M. Moore, A.D. Sutton, M. Schlaf, Conversion of furfural derivatives to 1,4-pentanediol and cyclopentanol in aqueous medium catalyzed by trans-[(2,9-Dipyridyl-1,10-phenanthroline)(CH₃CN)₂Ru](OTf)₂, *ACS Catal.* 10 (2020) 2667–2683, <https://doi.org/10.1021/acscatal.9b05055>.
- [12] R.M. Mironenko, O.B. Belskaya, V.P. Talsi, V.A. Likhonobov, Mechanism of Pd/C-catalyzed hydrogenation of furfural under hydrothermal conditions, *J. Catal.* 389 (2020) 721–734, <https://doi.org/10.1016/j.jcat.2020.07.013>.
- [13] P. Jia, X. Lan, X. Li, T. Wang, Highly selective hydrogenation of furfural to cyclopentanone over a NiFe bimetallic catalyst in a methanol/water solution with a solvent effect, *ACS Sustain. Chem. Eng.* 7 (2019) 15221–15229, <https://doi.org/10.1021/acssuschemeng.9b02112>.
- [14] Q. Deng, R. Gao, X. Li, J. Wang, Z. Zeng, J.-J. Zou, S. Deng, Hydrogenative ring-rearrangement of bio-based furanic aldehydes to cyclopentanone compounds over Pd/pyrochlore by introducing oxygen vacancies, *ACS Catal.* 10 (2020) 7355–7366, <https://doi.org/10.1021/acscatal.0c01666>.
- [15] M. Liu, L. Yuan, G. Fan, L. Zheng, L. Yang, F. Li, NiCu nanoparticles for catalytic hydrogenation of biomass-derived carbonyl compounds, *ACS Appl. Nano Mater.* 3 (2020) 9226–9237, <https://doi.org/10.1021/acsnano.0c01857>.
- [16] H.N. Pham, A.E. Anderson, R.L. Johnson, T.J. Schwartz, B.J. O'Neill, P. Duan, K. Schmidt-Rohr, J.A. Dumesic, A.K. Datye, Carbon overcoating of supported metal catalysts for improved hydrothermal stability, *ACS Catal.* 5 (2015) 4546–4555, <https://doi.org/10.1021/acscatal.5b00329>.
- [17] H.N. Pham, A.E. Anderson, R.L. Johnson, K. Schmidt-Rohr, A.K. Datye, Improved hydrothermal stability of mesoporous oxides for reactions in the aqueous phase, *Angew. Chem. Int. Ed.* 51 (2012) 13163–13167, <https://doi.org/10.1002/anie.201206675>.
- [18] J. Huo, J.-P. Tessonnier, B.H. Shanks, Improving hydrothermal stability of supported metal catalysts for biomass conversions: a review, *ACS Catal.* 11 (2021) 5248–5270, <https://doi.org/10.1021/acscatal.1c00197>.
- [19] H. Bergem, R. Xu, R.C. Brown, G.W. Huber, Low temperature aqueous phase hydrogenation of the light oxygenate fraction of bio-oil over supported ruthenium catalysts, *Green Chem.* 19 (2017) 3252–3262, <https://doi.org/10.1039/c7gc00367f>.
- [20] J. Huo, H.N. Pham, Y. Cheng, H.-H. Lin, L.T. Roling, A.K. Datye, B.H. Shanks, Deactivation and regeneration of carbon supported Pt and Ru catalysts in aqueous phase hydrogenation of 2-pentanone, *Catal. Sci. Technol.* 10 (2020) 3047–3056, <https://doi.org/10.1039/d0cy00163e>.
- [21] L. Li, N. Zhang, X. Huang, Y. Liu, Y. Li, G. Zhang, L. Song, H. He, Hydrothermal stability of core-shell Pd@Ce_{0.5}Zr_{0.5}O₂/Al₂O₃ catalyst for automobile three-way reaction, *ACS Catal.* 8 (2018) 3222–3231, <https://doi.org/10.1021/acscatal.8b00358>.
- [22] Y. Xu, G. Ma, J. Bai, Y. Du, C. Qin, M. Ding, Yolk@Shell FeMn@Hollow HZSM-5 nanoreactor for directly converting syngas to aromatics, *ACS Catal.* 11 (2021) 4476–4485, <https://doi.org/10.1021/acscatal.0c05658>.
- [23] C. Dong, Q. Yu, R.P. Ye, P. Su, J. Liu, G.H. Wang, Hollow carbon sphere nanoreactors loaded with PdCu nanoparticles: void-confinement effects in liquid-phase hydrogenations, *Angew. Chem. Int. Ed.* 59 (2020) 18374–18379, <https://doi.org/10.1002/anie.202007297>.
- [24] Z. Yu, N. Ji, J. Xiong, X. Li, R. Zhang, L. Zhang, X. Lu, Ruthenium nanoparticle-loaded hollow carbon spheres as nanoreactors for hydrogenation of levulinic acid: explicitly recognizing the void-confinement effect, *Angew. Chem. Int. Ed.* 60 (2021) 20786–20794, <https://doi.org/10.1002/anie.202107314>.
- [25] J. Lee, J.C. Park, H. Song, A nanoreactor framework of a Au@SiO₂ yolk/shell structure for catalytic reduction of p-nitrophenol, *Adv. Mater.* 20 (2008) 1523–1528, <https://doi.org/10.1002/adma.200702338>.
- [26] D. Dedovets, Q. Li, L. Leclercq, V. Nardello-Rataj, J. Leng, S. Zhao, M. Pera-Titus, Multiphase microreactors based on liquid-liquid and gas-liquid dispersions stabilized by colloidal catalytic particles, *Angew. Chem. Int. Ed.* 60 (2021) 2–25, <https://doi.org/10.1002/anie.202107537>.
- [27] E.D. Hernandez, B. Manookian, S.M. Auerbach, F.C. Jentoft, Shape-selective synthesis of alkylcyclopentenyl cations in zeolites and spectroscopic distinction of constitutional isomers, *ACS Catal.* 11 (2021) 12893–12914, <https://doi.org/10.1021/acscatal.1c03039>.
- [28] H. Cui, S. Liu, Y. Lv, S. Wu, L. Wang, F. Hao, P. Liu, W. Xiong, H. Luo, Transfer hydrogenation of cinnamaldehyde to cinnamyl alcohol in hydrophobically modified core-shell MOFs nanoreactor: identification of the formed metal–N as the structure of an active site, *J. Catal.* 381 (2020) 468–481, <https://doi.org/10.1016/j.jcat.2019.11.024>.
- [29] J. Lee, D.H.K. Jackson, T. Li, R.E. Winans, J.A. Dumesic, T.F. Kuech, G.W. Huber, Enhanced stability of cobalt catalysts by atomic layer deposition for aqueous-phase reactions, *Energy Environ. Sci.* 7 (2014) 1657–1660, <https://doi.org/10.1039/c4ee00379a>.

- [30] G. Zhou, H. Liu, K. Cui, A. Jia, G. Hu, Z. Jiao, Y. Liu, X. Zhang, Role of surface Ni and Ce species of Ni/CeO₂ catalyst in CO₂ methanation, *Appl. Surf. Sci.* 383 (2016) 248–252, <https://doi.org/10.1016/j.apsusc.2016.04.180>.
- [31] J. Shu, Y. Chen, S. Zhao, W. Chen, L. Shi, Y. Wang, J. Dong, Z. Li, F. Li, D. Li, Y. Li, Atomically dispersed ruthenium species inside metal–organic frameworks: combining the high activity of atomic sites and the molecular sieving effect of MOFs, *Angew. Chem. Int. Ed.* 58 (2019) 4271–4275, <https://doi.org/10.1002/anie.201814182>.
- [32] Y. Liu, B. Wang, Q. Fu, W. Liu, Y. Wang, L. Gu, D. Wang, Y. Li, Polyoxometalate-based metal–organic framework as molecular sieve for highly selective semi-hydrogenation of acetylene on isolated single Pd atom sites, *Angew. Chem. Int. Ed.* 60 (2021) 22522–22528, <https://doi.org/10.1002/anie.202109538>.